ACS Photonics

Article

pubs.acs.org/journal/apchd5

Optical Plasmons of Individual Gold Nanosponges

Cynthia Vidal,[†] Dong Wang,[‡] Peter Schaaf,[‡] Calin Hrelescu,*[,†] and Thomas A. Klar[†]

[†]Institute of Applied Physics, Johannes Kepler University Linz, 4040 Linz, Austria

[‡]Institute of Materials Engineering and Institute of Micro- and Nanotechnologies MacroNano, Technische Universität Ilmenau, 98693 Ilmenau, Germany

Supporting Information

ABSTRACT: The search for novel plasmonic nanostructures, which can act simultaneously as optical detectors and stimulators, is crucial for many applications in the fields of biosensing, electro- and photocatalysis, electrochemistry, and biofuel generation. In most of these areas, a large surface-to-volume ratio, as well as high density of active surface sites, is desirable. We investigate sponge-like, that is, fully porous, nanoparticles, called nanosponges, where both the gold and the air phase are fully percolated in three dimensions. We correlate, on a single nanoparticle basis, their optical scattering spectra (using dark field microscopy) with their individual morphology (using electron microscopy). We find that the scattering spectra of nanosponges depend only weakly on their size and outer shape, but are greatly influenced by their unique percolation, in qualitative agreement with numerical simulations.

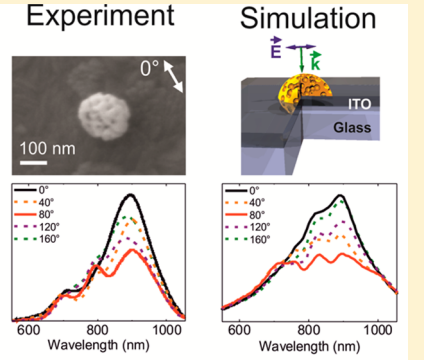

KEYWORDS: *plasmonics, mesoporous gold nanoparticles, localized surface plasmon resonance, nanoporosity, metamaterials*

Due to their fascinating plasmonic properties, noble metal nanoparticles have been actively studied over the last decades,[1] down to the single nanoparticle level.[2,3] The inherent shape and size dependence of their optical resonance frequency allows for spectral fine-tuning of the plasmon resonance or for creating plasmonic hotspots.[4−7] The manipulation of the plasmon resonance over a broad spectral range has become very important whenever plasmonic nanostructures are used in photonics, optoelectronics, bioanalysis, or biodiagnostics.[8−10] However, it turns out that, for many applications, most of the noble metal nanoparticles, which are commonly used for nanoplasmonics, do not exhibit simultaneously all the desirable properties, such as multiple plasmon resonances in the visible or NIR range of the spectrum, a high surface-to-volume ratio, and a high density of catalytic sites.

Specifically, for applications of noble metal nanostructures in the field of biosensing, a high surface-to-volume ratio together with multiple plasmon resonances in the visible or NIR range of the spectrum are crucial, for instance for surface-enhanced Raman scattering[11] or surface-enhanced IR spectroscopy.[12] Using conventionally shaped nanoparticles, a large surface-to-volume ratio can only be achieved for small particle sizes. This, however, raises two major problems: first, small nanoparticles (below 15 nm diameter) do not show a pronounced plasmon resonance because of a diminishing cross section, and second, a large surface-to-volume ratio heavily damps the plasmon resonance.[1] Only recently, research on complex-shaped nanoparticles such as nanostars[13] with large scattering cross sections but also an enlarged surface-to-volume ratio has started.

In this article, we investigate sponge-like gold nanoparticles that consist of gold and air filaments with dimensions between 15 and 25 nm, which are both fully percolated throughout the nanosponge. Two-dimensional nanoporous Au thin films have already been studied,[14] since they enable many catalytic and electrochemical applications.[15,16] Moreover, Au nanoporous membranes sustain both localized and propagating surface plasmon resonances.[17] In two dimensions, the plasmonic properties can be controlled via the membrane porosity.[18] While two dimensionally percolated metallic films are well studied, three dimensionally (3D) percolated nanoparticles are by far less well studied. Recently, efforts have been devoted to the fabrication and optical characterization of solid metal nanoparticles with surface dents[19] or of porous metallic shells.[20,21] Fully porous metallic nanoparticles have been produced,[22,23] however, the optical properties of individual nanosponges have not been investigated so far. Specifically, in the case of three-dimensionally percolated nanosponges, the investigation of optical spectra on the single nanosponge level is of utmost importance because each nanosponge possesses a unique, fully mesoporous structure. Hence, we correlate the optical scattering spectra (obtained by dark field spectroscopy) with the morphology of individual nanosponges (obtained by electron microscopy) and we find that the scattering spectra of nanosponges depend very much on their individual, fully percolated structure.

RESULTS AND DISCUSSION

Morphology of the Nanosponges. The nanosponges were fabricated via dewetting/dealloying of a silver−gold (Ag−

Received: May 23, 2015
Published: September 8, 2015

DOI: 10.1021/acsphotonics.5b00281
ACS Photonics 2015, 2, 1436−1442

Au) bilayer as reported previously.[22] Briefly, one silver layer and one gold layer are deposited on a silicon wafer covered with silica. Annealing leads to dewetting and to the formation of Ag−Au alloy nanoparticles. The nanoparticles consist of well-mixed gold and silver. Submersion into a solution of nitric acid removes the silver, while the gold forms percolated filaments. The ligament size depends on Ag concentration in the Au−Ag alloy (or layer thickness ratio of the Ag and Au thin films before dewetting) as well as concentration and temperature of the HNO_3 solution. However, reproducibility (mean particle size, particle size distribution, ligament size) is good if all experimental parameters remain the same. The percolated gold filaments provide a surface area around 10^5 m^2/g.[22]

Figure 1a presents a scanning electron microscope (SEM) image of a few nanosponges on a silica/silicon (SiO_2/Si)

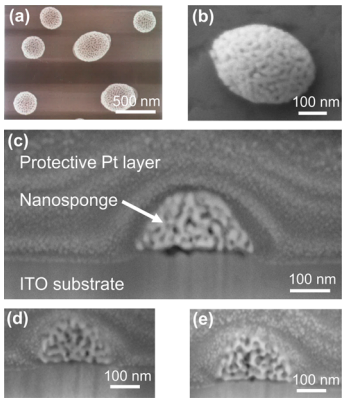

Figure 1. SEM images of three-dimensionally Au−air percolated nanosponges. (a) Nanosponges on a SiO_2/Si substrate. (b) Single nanosponge after transfer onto an ITO substrate. (c−e) Cross sections after subsequent FIB milling of the nanosponge in (b), protected by a platinum (Pt) layer.

substrate with approximately 1.2×10^{10} nanosponges on a 4 in. wafer. Histograms of the nanosponges' diameter and autocorrelation functions of nanosponges on a silicon wafer are presented in Figure S1 in the Supporting Information. In order to perform single particle spectroscopy, the nanosponges were transferred from the original SiO_2/Si substrate onto a transparent tin-doped indium oxide (ITO) substrate, which was prepatterned with a chess board like coordinate system. This coordinate system allowed us to locate individual nanosponges in the SEM and in the dark field microscope in order to correlate morphology and single nanoparticle scattering spectra. A typical Au nanosponge on an ITO substrate is shown in Figure 1b. In this particular case, the particle's surface exhibits a mesoporous topology with Au filaments of approximately 22 ± 5 nm in diameter separated by 18 ± 5 nm air holes (Figure 1a,b). For more details, see the Experimental Section.

In order to reveal the interior structure of the nanosponges, they were sliced by focused ion beam (FIB) milling. A protective, conductive platinum (Pt) layer of several hundred nanometers was first deposited atop the Au nanosponge to prevent its disaggregation or damage by the FIB. The ion beam was then focused perpendicularly to the substrate and milled the protective layer, nanosponge and substrate in a raster pattern. The particle's cross sections were imaged after each milling step by SEM, which was tilted under 54° with respect to the FIB stage. Figure 1c−e shows SEM images of the internal structure of the Au nanosponge from Figure 1b after three consecutive milling steps. Each cross section reveals that the nanosponge exhibits a porous Au−air arrangement, with a similar porosity (Au−air filaments size), as observed on the surface of the particle, within and throughout its entire volume.

White-Light Scattering Spectra of Single Nanosponges. In order to investigate the influence of the 3D Au−air percolation on the optical properties, white-light scattering spectra of single nanosponges were measured. First, the exact location of an individual Au nanosponge on the ITO substrate was pinpointed by SEM imaging with the help of the coordinate system, and afterward, the scattering spectrum of the same individual Au nanosponge was recorded using dark field spectroscopy.[24]

Figure 2a−d shows SEM images (left) of spheroidal Au nanosponges and their corresponding scattering spectra (right).

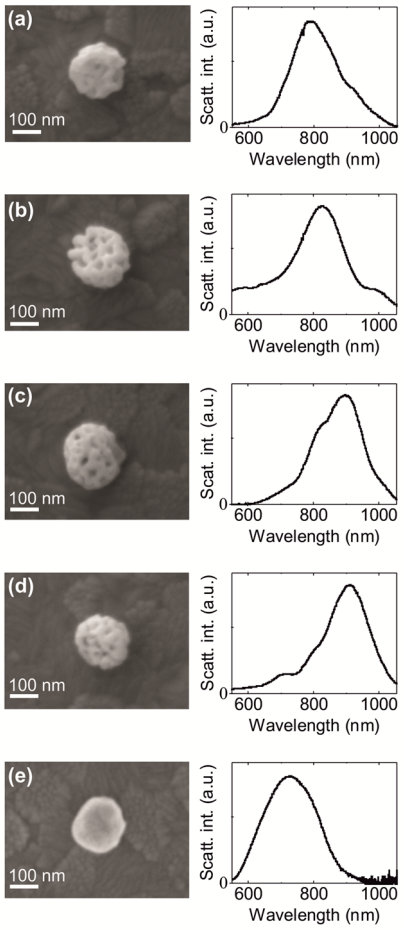

Figure 2. (a−d) SEM images of individual nanosponges (diameter ca. 200 nm; left) and corresponding scattering spectra (right). Particles with comparable size and porosity show distinctly different scattering spectra because of their specific inner structure. (e) SEM image of a solid Au nanoparticle (diameter ca. 200 nm; left) and corresponding scattering spectra (right).

For the time being, unpolarized light was used for illumination, and no polarizer was applied in front of the detector. The SEM images show that the nanosponges have quite similar sizes (between 195 and 230 nm) and porosity (20 ± 5 nm diameter Au filaments and 22 ± 5 nm air holes). The nanosponge in Figure 2a has a diameter of 195 nm and a scattering maximum at 790 nm and the nanosponge in Figure 2b measures 215 nm

DOI: 10.1021/acsphotonics.5b00281
ACS Photonics 2015, 2, 1436−1442

in diameter and exhibits a scattering maximum at 825 nm. The nanosponge in Figure 2c has an elliptic cross section with dimensions of 210 and 230 nm along the principal axes and a scattering maximum at 900 nm, while the nanosponge in Figure 2d has a diameter of 195 nm and a scattering maximum at 905 nm. Remarkably, the Au nanosponges presented in Figure 2a and d both measure 195 nm in diameter but have very different scattering maxima at 790 and 905 nm, respectively. Additional examples for the correlation of the morphology of individual nanosponges with corresponding unpolarized scattering spectra are presented in the Supporting Information, Figure S2.

The dark field measurements in Figure 2a–d illustrate that, compared to solid spherical Au nanoparticles of similar size (Figure 2e),[1,25,26] the scattering of the Au nanosponges is red-shifted. A similar behavior was observed for the extinction spectra of Au nanoparticles with dents on the surface[19] or roughened Au shells[20] in ensemble averaged measurements. Nevertheless, our results clearly show that, even though the four Au nanosponges in Figure 2a–d have similar diameters (205 ± 10 nm) and a similar porosity, that is, Au ligament sizes, their scattering maxima are positioned at notably different wavelengths. This behavior contrasts with that of solid Au nanospheres and indicates that the Au nanosponges scatter mainly independently of the shape of their envelope and their diameter. Therefore, the scattering spectra are unique to each nanosponge, a fact that would have been hidden by ensemble measurements. It implies that the specific 3D Au/air percolation pattern is responsible for the individual optical properties of each nanosponge.

Polarization-Dependent Scattering Spectra of Single Nanosponges. Next, we concentrate on polarization-dependent scattering spectra of individual Au nanosponges. The illumination was unpolarized, but a linear polarizer was inserted in front of the spectrometer. Figure 3 shows the SEM images

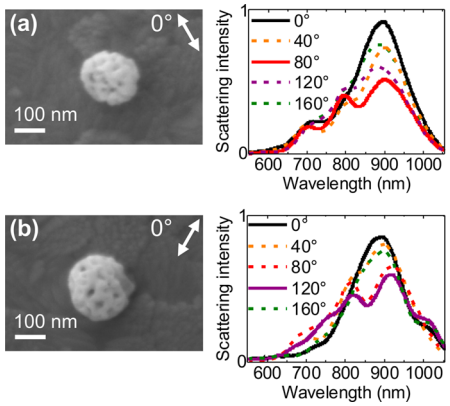

Figure 3. SEM images (left) and polarization-dependent scattering spectra (right) of (a) a 195 nm nanosponge and (b) a 220 nm nanosponge. The double arrows in the SEM images represent the 0° polarization axis. The polarizer axis was rotated clockwise in 20° steps but, for clarity, only 40° steps are shown here.

(left) and the corresponding polarization-dependent scattering spectra (right) of a 195 nm Au nanosponge (Figure 3a) and a 220 nm Au nanosponge (Figure 3b), both having a spheroidal shape. The polarizer axis was rotated clockwise in 20° steps, but for clarity the spectra are presented in 40° polarization steps. The double arrows in the SEM images represent the 0° direction of the polarizer axis for the corresponding dark field measurement. The complete data set with 20° polarization stepping as well as examples of additional nanosponges are shown in the Supporting Information, Figure S2.

The polarization-dependent scattering spectra of the smaller Au nanosponge in Figure 3a reveals three maxima at approximately 700, 800, and 900 nm. The maxima at 700 and 800 nm keep roughly the same intensity for each polarization direction, whereas the peak at 900 nm reaches a maximum intensity for 0° polarization and a minimum for 80° polarization.

The polarization-dependent scattering spectra of the larger Au nanosponge in Figure 3b exhibits four maxima at approximately 700, 820, 890, and 920 nm. The peak at 700 nm shows a maximum intensity for 80° polarization and a minimal intensity for 0° polarization. The peak at 890 nm has its maximum intensity at 0° polarization and splits into two peaks at 820 and 920 nm for 80° polarization. Both peaks reach their minimum intensity for 120° polarization. Each nanosponge exhibits unique polarization-dependent scattering spectra, although both show a similar degree of porosity and similar shape and diameters. More examples are shown in Figure S3 in the Supporting Information.

Figure 3 clearly shows that, even though the nanosponges have the same size and average porosity, individual spheroidal nanosponges exhibit different polarization-dependent scattering spectra. The exact arrangement of the Au and air filaments within the nanosponges is specific for each nanosponge. This unique random and inhomogeneous distribution of the Au filaments in the volume of the nanosponge is the origin of the anisotropy inducing the individual polarization-dependent scattering spectra. The polarization-dependent spectra in Figure 3 reveal multiple maxima at several distinct wavelengths, which we attribute to multiple plasmonic contributions arising from localized plasmon resonances of the Au filaments and coupling between these resonances throughout the nanosponge. Similar behavior was observed on porous Au thin films.[27] The observed optical response of the Au nanosponges seems to depend on the interaction of several locally excited plasmonic modes that can be decomposed via polarization.[28] Such interpretation explains the spectrally broad resonances and the diverse scattering responses of the Au nanosponges in the unpolarized measurements (Figures 2) as well as the multiple plasmonic resonances observed in the polarization-dependent measurements (Figure 3). Notably, it also means that the plasmonic eigenmodes of each nanosponge, underlying the overall spectra, are sharper than the polarization-averaged response. Such sharp resonances are a strong hint that losses are indeed not very pronounced, despite a large surface-to-volume ratio, which is prone to induce surface damping effects.[1] However, the fact that the scattering peaks fluctuate upon tuning the polarizer indicates that it is not possible to consider individual nanosponges as a homogeneous effective (meta)material with a well-defined dielectric constant.

Numerical Modeling of Single Nanosponges. In order to underline our experimental findings on the percolation-dependent optical properties of the Au nanosponges, three-dimensional finite difference time domain (FDTD) calculations were performed. Here, we have used the commercially available FDTD solver from Lumerical Solutions Inc. Since numerical modeling of a 3D percolation pattern of a specific nanosponge would be extremely difficult in terms of computational efforts and is practically impossible, as even a FIB crosscut would hardly give the exact inner pattern, we restricted ourselves to a simpler model. In order to mimic the experimental conditions

DOI: 10.1021/acsphotonics.5b00281
ACS Photonics 2015, 2, 1436–1442

best as possible, the nanosponges were emulated as Au half-spheres (compare Figure 1c) on an ITO substrate with a diameter of 195 nm, similar to the nanosponges in Figures 2d and 3a. For the excitation, a plane wave with the same spectral bandwidth as in the experiments was used. Furthermore, the Au half-spheres are perforated by randomly distributed air spheres. In the SEM images, the so-called edge effect leads to an increased secondary electron emission from the metallic filaments,[29] thus, the diameter of the air holes, as they appear in the SEM images, is underestimated. Considering this, we set the diameter of the air holes to 24 nm in the simulations. The air spheres are allowed to overlap by 20% in all directions. This allows for the formation of air filaments that reach throughout the nanosponge, so that the modeled nanosponges are suitable imitations of 3D Au−air percolation.

A total number of 146 air spheres distributed randomly through the whole Au half-sphere was chosen under two considerations: first, the number of spheres on the Au half-sphere surface is 76, which is the average number of air holes visible in the SEM images of individual nanosponges, and second, the air−Au volume ratio is between 40 and 50%, depending on the individual random distribution of the air spheres. Similar volume ratios can be deduced from the FIB crosscuts (Figure 1c−e). By using a random generator, we ensure that the distribution of the air spheres throughout the whole nanosponge is different in each run of simulation, while the rest of the simulation parameters are kept the same. In order to investigate the dependence of scattering spectra on the unique percolation of the nanosponges, we performed calculations for several model nanosponges, that is, several different random distributions of the air spheres. Several examples of calculated unpolarized scattering spectra of individual nanosponges as well as the calculated spectrum of a solid gold half-sphere can be found in the Supporting Information, Figure S3. In the main text, we would like to proceed directly to polarized illumination.

Figure 4a displays the schematics of the model nanosponge (left) and the calculated scattering spectra (i.e., scattering cross section) for a normal incident plane wave excitation and different incident polarizations (right). For clarity, we only show polarizations rotated in 40° steps (see Figure S4a in the Supporting Information for more incident polarization directions).

Comparing the calculated scattering spectra from Figure 4a with the measured scattering spectra in Figure 3, one immediately observes that multiple maxima at several distinct wavelengths as well as polarization-dependent scattering spectra are qualitatively reproduced in the calculations.

The fact that nanoparticles with the same diameter show different scattering spectra (cf. Figure 2a,d) and that the scattering spectrum of a spherical nanosponge is highly sensitive to the polarization (Figure 3) might also be explained by a pure surface roughness of nanoparticles with dents. Therefore, we calculated the polarization-dependent scattering spectra for the same geometry, a gold half-sphere of 195 nm diameter on an ITO substrate. However, in contrast to the previous model (Figure 4a), the air spheres are now distributed only on the surface of the Au half-sphere, thus, forming surface dents, while the interior of the nanoparticle is solid gold, as sketched in Figure 4b (left). Furthermore, for a fair comparison with the previous case in Figure 4a, we kept the exact same distribution of 76 air spheres on the surface of the Au half-sphere and deleted only the air spheres previously distributed in

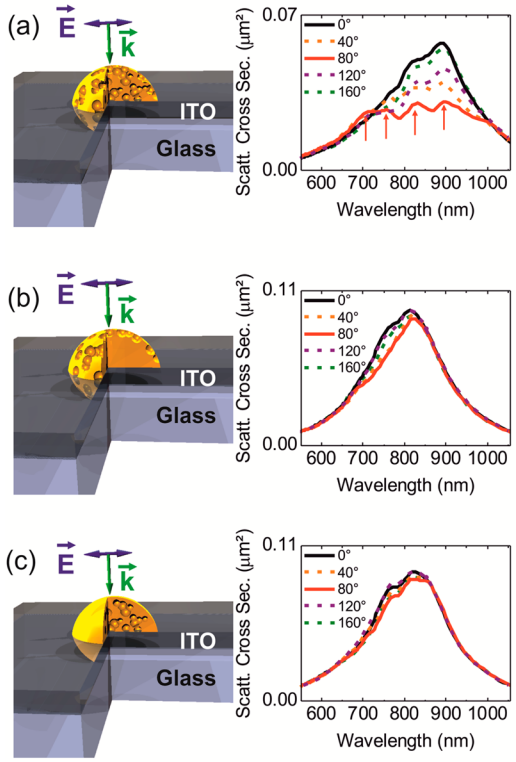

Figure 4. Numerical modeling of single nanosponges: Schematics of the model nanosponges (left) and the calculated scattering spectra (i.e., scattering cross section) for normal incident plane wave excitation and different incident polarizations (right). The nanosponges were modeled as gold half-spheres of 195 nm in diameter on an ITO substrate and are perforated by randomly distributed air spheres of 24 nm in diameter. (a) Nanosponge: the air spheres are distributed randomly throughout the whole gold half-sphere. (b) Nanoparticle with surface dents only: the air spheres are distributed only on the surface of the gold half-sphere, but the interior is solid gold. (c) Nanoparticle with porous interior: the air spheres are distributed only in the interior of the gold half-sphere, while the surface is smooth.

the interior of the Au half-sphere. The corresponding polarization resolved scattering cross sections are shown in Figure 4b (right). The presented numerical spectra in Figure 4b exhibit rather low sensitivity to polarization. Therefore, one can conclude that the optical properties of nanosponges are not dominated by their surface structure. Next, we also computed the polarization-dependent scattering spectra for a smooth Au half-sphere surface with a porous interior, as sketched in Figure 4c (left). In this model, all air spheres that connect to the surface were deleted, while the distribution of air spheres in the interior of the Au half-sphere is identical to the distribution used in the model in Figure 4a. Figure 4c (right) displays the corresponding scattering cross sections. Again, the calculated spectra exhibit rather low sensitivity to polarization compared to the case of a full 3D percolation (for even more incident polarizations and additional examples see Supporting Information, Figures S6 and S7). Therefore, we conclude that the strong polarization dependence of the scattering spectra observed in the experiments is neither purely caused by the surface dents nor solely caused by the porous interior of the nanosponges. The experimental findings can only be qualitatively reproduced by simulations when the surface dents together with the porous interior are forming air channels

DOI: 10.1021/acsphotonics.5b00281
ACS Photonics 2015, 2, 1436−1442

or filaments that connect to the surface and penetrate throughout the whole interior. In order to illustrate this, the distributions of field enhancement at wavelengths corresponding to the different maxima of the polarization-dependent scattering spectra were calculated.

Figure 5 shows the distribution of the field enhancement inside and outside of the nanosponge from Figure 4a calculated

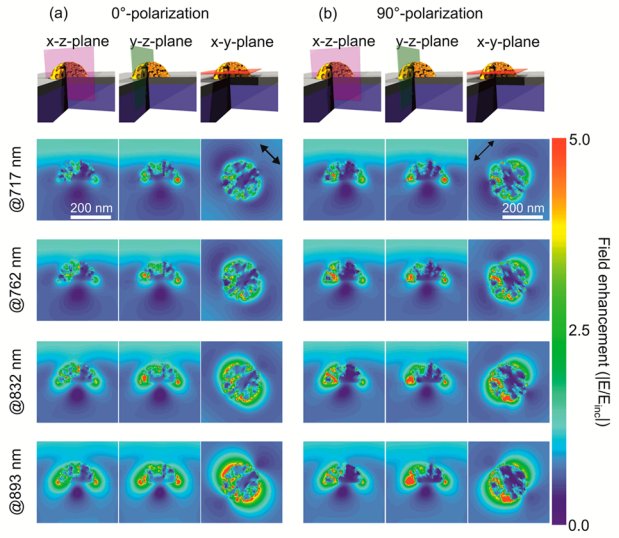

Figure 5. Calculated field enhancement distributions inside the nanosponge from Figure 4a for 0° (a) and 90° incident polarization (b) evaluated at the plasmon resonances indicated by the red arrows in Figure 4a. The planes of the cross-cuts are sketched in the upper panels. The $x-z$ and $y-z$ planes are perpendicular to the substrate and intersect the nanosponge at its center, while the $x-y$ plane is 20 nm above the nanosponge center and parallel to the substrate. The black arrows indicate the incident polarization.

for 0° and 90° incident polarization. Precisely, it shows the absolute value of the local field, **E**, compared to the incoming field $\mathbf{E}_{inc}$. The field distribution was evaluated at wavelengths corresponding to the different scattering maxima indicated by the arrows in Figure 4a, namely, at 717, 762, 832, and 893 nm. For a better visualization of the field distributions, three cross-cuts through the nanosponge are shown, denoted as $x-z$, $y-z$, and $x-y$ planes. As sketched in Figure 5, the $x-z$ and $y-z$ planes are cross-cuts through the center of the nanosponge in the x or y direction perpendicular to the substrate, respectively. The $x-y$ cut is 20 nm above the ITO substrate. The distribution of the hot spots, that is, where the field is highest, is varying for different wavelengths and polarization directions.

The simulated field enhancements in Figure 5, specifically those for the longer wavelengths, look basically similar to plasmonic modes of homogeneous nanoparticles; however, they are heavily disturbed by the inner structure of the nanosponges. For instance, in the case of 0° polarization and 893 nm emission, the field is enhanced at the two opposing surfaces, as can be seen in the upper left area and the lower right area of the (x,y) cut, in correspondence to the direction of the polarization (see double arrow), and there exists a nodal plane perpendicular to it. Notably, however, there are many hot spots of enhanced fields throughout the interior of the nanosponge. In the case of 90° rotated polarization (but still considering the wavelength of 893 nm), the distribution of hot spots is less symmetric in the (x,y) cut than that at 0° polarization. While in the case of 0° polarization, the hot spots in the upper left and lower right area are of comparable intensity and density; in the case of 90° polarization, the lower left area contains more hot spots that are also, on average, more intense than the hot spots in the upper right area. Hence, at 893 nm, the 0° polarization induces a more dumbbell-shaped distribution of hot spots, which apparently couple more strongly to the scattered field than in the case of 90° polarization. This is apparent in Figure 4a, where the scattered intensity at 893 nm is much stronger for 0° polarization than for 90° polarization. A possible explanation could be that the 0° polarization plasmon contains more dipole character, which couples effectively to propagating light, while the more asymmetric distribution in the case of 90° polarization couples less, and indeed, the scattering at 893 nm is weaker in the case of 90° polarization than in the case of 0° polarization, cf. Figure 4a.

In the case of 717 nm, the overall field distribution does show a higher order symmetry, as it is expected for a shorter wavelength resonance. However, it is very difficult to assign a specific symmetry due to the multiple individual hot spots. With great caution, one might interpret the pattern as a heavily disturbed quadrupolar or even higher order resonance, which is nevertheless allowed to couple to propagating fields via mediation of the hot spots within the nanosponges. Notably, it is apparent that the distribution and the intensity of the hot spots are similar for both orthogonal polarizations. Hence, one would expect a similar coupling to propagating fields and, indeed, the scattering intensity at 717 nm, which is shown in Figure 4a, is similar for each polarization. The resonances at 832 and 762 nm are probably other interferences of an overall nanoparticle plasmon and internal plasmonic resonances. Again, one observes that the more symmetric distributions of hot spots in the case of 0° polarization tend to a stronger coupling to the scattered field than the less symmetric distributions in the case of 90° polarization.

CONCLUSION

In summary, we have shown that the optical properties of nanosponges are strongly influenced by their unique 3D Au–air percolation pattern. Slicing the Au nanosponges using FIB milling showed that they are truly three-dimensionally mesoporous. The experimentally and numerically investigated scattering spectra of individual Au nanosponges yield that their optical behavior is mostly independent of their diameter, outer shape, and surface roughness, but strongly dependent on their exact and unique three dimensionally percolated structure. Indeed, the inhomogeneity and anisotropy of the hot spots observed in the simulation as well as the polarization dependence of the scattering spectra show that it is not possible to consider a single Au nanosponge as an isotropic effective medium. These findings suggest that the observed scattering spectra correspond to dipolar, as well as higher order modes, substantially disturbed by locally excited plasmonic modes that couple throughout each nanosponge. The plasmonic properties of the nanosponges, in combination with their large surface-to-volume ratio, may bring substantial advantages for applications such as in surface-enhanced Raman scattering (SERS),[11] surface-enhanced infrared spectroscopy (SEIRA),[12] or the possible use of nanosponges in photo- and electrocatalysis,[30,31] the generation of biofuel[32] or steam[33] or as nanoscale electrodes in electrochemistry.[34]

DOI: 10.1021/acsphotonics.5b00281
ACS Photonics 2015, 2, 1436–1442

EXPERIMENTAL SECTION

Morphology and Inner Structure Characterization. The SEM images and the FIB milling were performed with a ZEISS 1540XB CrossBeam. The secondary electron (SE) detector was used for the SEM images. In order to avoid damaging of the nanosponges and to obtain the best possible surface structure images, the working distance was 10 mm and the acceleration voltage was 5 kV. The instrumental settings were the best feasible compromise between reasonable material and topographic contrast and resolution.

For the estimation of the size of the gold filaments and air holes of a particular nanosponge, the SEM images were analyzed with the free software *Gwyddion*.[35] Considering the so-called edge effect,[29] which leads to an increased secondary electron emission from the Au filaments, the Au filaments appear much bigger in the SEM images than they really are, hence, the real size of the air holes is obscured. In order to derive the dimensions of the gold filaments and of the air holes, we analyzed the secondary electron intensities along a line comprising several Au filaments and air holes. For the Au filaments, we defined the diameter as the distance between the two points along the line which show equally strong secondary electron emission with an intensity of half the maximal secondary electron emission intensity of the gold filaments. The dimensions of the air holes were derived similarly, but the considered distance was the distance between points along the line, which had equally strong secondary electron emission with intensity of half the minimal secondary electron emission intensity.

Optical Characterization. The samples were studied on an inverted dark field microscope, which allows recording of white light scattering spectra from single particles on a spectrometer (Acton SpectraPro SP2150) equipped with a Peltier cooled charge-coupled device camera (Andor IDus). A halogen microscopy lamp (150 W) without an IR filter was used for excitation. The scattering spectra were corrected for background, instrument response function, and the excitation source spectrum.

Numerical Modeling. The scattering cross section of the nanosponges were calculated using the commercial software FDTD Solutions (version 8.9.269) from Lumerical Solutions Inc., which provides a 3D Maxwell equation solver based on Finite-Difference Time-Domain method (FDTD). The simulated nanosponges consist of a Au half-sphere (diameter 195 nm) perforated by randomly distributed air spheres of 24 nm diameter on an ITO substrate in air. A random generator script was used to distribute 146 air spheres in such a way that the 3D percolation could be mimicked best achievable. Therefore, we defined four concentric half-sphere surfaces on which a particular number of air spheres is randomly distributed. The first half-sphere surface in the stack is the outer surface of the Au half-sphere. The radii of the individual half-spheres defining the other three surfaces within the stack were chosen in such a way that air spheres distributed on two adjacent half-sphere surfaces may overlap by 20%. The air spheres on the same half-sphere surface were allowed to overlap by 20% as well. This allows for the formation of air filaments that reach throughout the nanosponge. The random seed generator was reset based on the system time (clock time) for each sphere distribution on a specific half-sphere surface. Furthermore, we ensured that 76 air spheres, the average number of the air holes visible in the SEM images of individual nanosponges, were distributed on the Au half-sphere surface. In the modeling, the permittivity of gold was obtained by a generalized multicoefficient fit of the permittivity of bulk gold according to Johnson and Christy.[36] The substrate was modeled as a 100 nm thick ITO film on glass. The glass is covering one-half-space of the simulation volume. The Total Field/Scattered Field (TFSF) source implemented in the software was used as excitation source. The excitation direction was vertically incident to the substrate from the air half-space of the simulation volume. For the permittivity of ITO, a FDTD multicoefficient fit to the data from ref 37 was used.

ASSOCIATED CONTENT

Supporting Information

The Supporting Information is available free of charge on the ACS Publications website at DOI: 10.1021/acsphotonics.5b00281.

Additional supporting data (PDF)

AUTHOR INFORMATION

Corresponding Author

*E-mail: calin.hrelescu@jku.at.

Notes

The authors declare no competing financial interest.

ACKNOWLEDGMENTS

The authors would like to thank Heidi Piglmayer-Brezina and Günter Hesser for technical support on SEM and FIB, Dmitry Sivun for discussion, and Jaroslaw Jacak and Johannes Ziegler for critical reading. This work was financially supported by the European Research Council (ERC Starting Grant 257158 "Active NP") and Deutsche Forschungsgemeinschaft (DFG, Grant SCHA 632/20-1).

REFERENCES

(1) Kreibig, U.; Vollmer, M. *Optical Properties of Metal Clusters*; Springer: Berlin, 1995.

(2) Krenn, J. R.; Gotschy, W.; Somitsch, D.; Leitner, A.; Aussenegg, F. R. Investigation of Localized Surface Plasmons with the Photon Scanning Tunneling Microscope. *Appl. Phys. A: Mater. Sci. Process.* **1995**, *61*, 541−545.

(3) Klar, T.; Perner, M.; Grosse, S.; von Plessen, G.; Spirkl, W.; Feldmann, J. Surface-Plasmon Resonances in Single Metallic Nanoparticles. *Phys. Rev. Lett.* **1998**, *80*, 4249−4252.

(4) Averitt, R. D.; Sarkar, D.; Halas, N. J. Plasmon Resonance Shifts of Au-Coated Au2S Nanoshells: Insight into Multicomponent Nanoparticle Growth. *Phys. Rev. Lett.* **1997**, *78*, 4217−4220.

(5) Jana, N. R.; Gearheart, L.; Murphy, C. J. Wet Chemical Synthesis of Silver Nanorods and Nanowiresof Controllable Aspect Ratio. *Chem. Commun.* **2001**, 617−618.

(6) Kelly, K. L.; Coronado, E.; Zhao, L. L.; Schatz, G. C. The Optical Properties of Metal Nanoparticles: The Influence of Size, Shape, and Dielectric Environment. *J. Phys. Chem. B* **2003**, *107*, 668−677.

(7) Nehl, C. L.; Liao, H.; Hafner, J. H. Optical Properties of Star-Shaped Gold Nanoparticles. *Nano Lett.* **2006**, *6*, 683−688.

(8) Maier, S. A.; Kik, P. G.; Atwater, H. A.; Meltzer, S.; Harel, E.; Koel, B. E.; Requicha, A. A. G. Local Detection of Electromagnetic Energy Transport below the Diffraction Limit in Metal Nanoparticle Plasmon Waveguides. *Nat. Mater.* **2003**, *2*, 229−232.

(9) Rosi, N. L.; Mirkin, C. A. Nanostructures in Biodiagnostics. *Chem. Rev.* **2005**, *105*, 1547−1562.

(10) Dionne, J. A.; Sweatlock, L. A.; Atwater, H. A.; Polman, A. Plasmon Slot Waveguides: Towards Chip-Scale Propagation with

DOI: 10.1021/acsphotonics.5b00281
ACS Photonics 2015, 2, 1436−1442

Subwavelength-Scale Localization. *Phys. Rev. B: Condens. Matter Mater. Phys.* **2006**, *73*, 035407.
(11) Kneipp, J.; Kneipp, H.; Kneipp, K. SERS-a Single-Molecule and Nanoscale Tool for Bioanalytics. *Chem. Soc. Rev.* **2008**, *37*, 1052−1060.
(12) Enders, D.; Rupp, S.; Küller, A.; Pucci, A. Surface Enhanced Infrared Absorption on Au Nanoparticle Films Deposited on SiO_2/Si for Optical Biosensing: Detection of the Antibody−antigen Reaction. *Surf. Sci.* **2006**, *600*, L305−L308.
(13) Hrelescu, C.; Sau, T. K.; Rogach, A. L.; Jaeckel, F.; Laurent, G.; Douillard, L.; Charra, F. Selective Excitation of Individual Plasmonic Hotspots at the Tips of Single Gold Nanostars. *Nano Lett.* **2011**, *11*, 402−407.
(14) Gadenne, P.; Beghdadi, A.; Lafait, J. Optical Cross-over Analysis of Granular Gold Films at Percolation. *Opt. Commun.* **1988**, *65*, 17−21.
(15) Cortie, M. B.; Maaroof, A. I.; Smith, G. B. Electrochemical Capacitance of Mesoporous Gold. *Gold Bull.* **2005**, *38*, 14−22.
(16) Qiu, H.-J.; Li, X.; Xu, H.-T.; Zhang, H.-J.; Wang, Y. Nanoporous Metal as a Platform for Electrochemical and Optical Sensing. *J. Mater. Chem. C* **2014**, *2*, 9788−9799.
(17) Yu, F.; Ahl, S.; Caminade, A.-M.; Majoral, J.-P.; Knoll, W.; Erlebacher, J. Simultaneous Excitation of Propagating and Localized Surface Plasmon Resonance in Nanoporous Gold Membranes. *Anal. Chem.* **2006**, *78*, 7346−7350.
(18) Maaroof, A. I.; Gentle, A.; Smith, G. B.; Cortie, M. B. Bulk and Surface Plasmons in Highly Nanoporous Gold Films. *J. Phys. D: Appl. Phys.* **2007**, *40*, 5675.
(19) Zhang, Q.; Large, N.; Nordlander, P.; Wang, H. Porous Au Nanoparticles with Tunable Plasmon Resonances and Intense Field Enhancements for Single-Particle SERS. *J. Phys. Chem. Lett.* **2014**, *5*, 370−374.
(20) Wang, H.; Goodrich, G. P.; Tam, F.; Oubre, C.; Nordlander, P.; Halas, N. J. Controlled Texturing Modifies the Surface Topography and Plasmonic Properties of Au Nanoshells. *J. Phys. Chem. B* **2005**, *109*, 11083−11087.
(21) Qiu, H.-J.; Peng, L.; Li, X.; Xu, H. T.; Wang, Y. Using Corrosion to Fabricate Various Nanoporous Metal Structures. *Corros. Sci.* **2015**, *92*, 16−31.
(22) Wang, D.; Schaaf, P. Nanoporous Gold Nanoparticles. *J. Mater. Chem.* **2012**, *22*, 5344.
(23) Li, X.; Chen, Q.; McCue, I.; Snyder, J.; Crozier, P.; Erlebacher, J.; Sieradzki, K. Dealloying of Noble-Metal Alloy Nanoparticles. *Nano Lett.* **2014**, *14*, 2569−2577.
(24) Sönnichsen, C.; Franzl, T.; Wilk, T.; von Plessen, G.; Feldmann, J.; Wilson, O.; Mulvaney, P. Drastic Reduction of Plasmon Damping in Gold Nanorods. *Phys. Rev. Lett.* **2002**, *88*, 077402.
(25) Mie, G. Beiträge zur Optik trüber Medien, speziell kolloidaler Metallösungen. *Ann. Phys.* **1908**, *330*, 377−445.
(26) Maier, S. A. *Plasmonics: Fundamentals and Applications*; Springer: New York, 2007.
(27) Bosman, M.; Anstis, G. R.; Keast, V. J.; Clarke, J. D.; Cortie, M. B. Light Splitting in Nanoporous Gold and Silver. *ACS Nano* **2012**, *6*, 319−326.
(28) Barrow, S. J.; Rossouw, D.; Funston, A. M.; Botton, G. A.; Mulvaney, P. Mapping Bright and Dark Modes in Gold Nanoparticle Chains Using Electron Energy Loss Spectroscopy. *Nano Lett.* **2014**, *14*, 3799−3808.
(29) Richards, R. G.; Owen, G. R.; Ap Gwynn, I. Low Voltage Backscattered Electron Imaging (< 5kV) Using Field Emission Scanning Electron Microscopy. *Scanning Microsc.* **1999**, *13*, 55−60.
(30) Kochuveedu, S. T.; Jang, Y. H.; Kim, D. H. A Study on the Mechanism for the Interaction of Light with Noble Metal-Metal Oxide Semiconductor Nanostructures for Various Photophysical Applications. *Chem. Soc. Rev.* **2013**, *42*, 8467−8493.
(31) Jing, C.; Rawson, F. J.; Zhou, H.; Shi, X.; Li, W.-H.; Li, D.-W.; Long, Y.-T. New Insights into Electrocatalysis Based on Plasmon Resonance for the Real-Time Monitoring of Catalytic Events on Single Gold Nanorods. *Anal. Chem.* **2014**, *86*, 5513−5518.
(32) van de Krol, R.; Liang, Y.; Schoonman, J. Solar Hydrogen Production with Nanostructured Metal Oxides. *J. Mater. Chem.* **2008**, *18*, 2311−2320.
(33) Neumann, O.; Urban, A. S.; Day, J.; Lal, S.; Nordlander, P.; Halas, N. J. Solar Vapor Generation Enabled by Nanoparticles. *ACS Nano* **2013**, *7*, 42−49.
(34) Dondapati, S. K.; Ludemann, M.; Müller, R.; Schwieger, S.; Schwemer, A.; Händel, B.; Kwiatkowski, D.; Djiango, M.; Runge, E.; Klar, T. A. Voltage-Induced Adsorbate Damping of Single Gold Nanorod Plasmons in Aqueous Solution. *Nano Lett.* **2012**, *12*, 1247−1252.
(35) *Gwyddion*, Free SPM (AFM, SNOM/NSOM, STM, MFM) Data Analysis Software; Czech Metrology Institute: Brno, Czech Republic, 2015.
(36) Johnson, P. B.; Christy, R. W. Optical Constants of the Noble Metals. *Phys. Rev. B* **1972**, *6*, 4370−4379.
(37) König, T. A. F.; Ledin, P. A.; Kerszulis, J.; Mahmoud, M. A.; El-Sayed, M. A.; Reynolds, J. R.; Tsukruk, V. V. Electrically Tunable Plasmonic Behavior of Nanocube−Polymer Nanomaterials Induced by a Redox-Active Electrochromic Polymer. *ACS Nano* **2014**, *8*, 6182−6192.

DOI: 10.1021/acsphotonics.5b00281
ACS Photonics 2015, 2, 1436−1442